

Ultrasound transmission tomography image reconstruction with a fully convolutional neural network

Zhao, Wenzhao; Wang, Hongjian; Gemmeke, Hartmut; Van Dongen, Koen W.A.; Hopp, Torsten; Hesser, Jürgen

DOI

[10.1088/1361-6560/abb5c3](https://doi.org/10.1088/1361-6560/abb5c3)

Publication date

2020

Document Version

Final published version

Published in

Physics in Medicine and Biology

Citation (APA)

Zhao, W., Wang, H., Gemmeke, H., Van Dongen, K. W. A., Hopp, T., & Hesser, J. (2020). Ultrasound transmission tomography image reconstruction with a fully convolutional neural network. *Physics in Medicine and Biology*, 65(23), Article 235021. <https://doi.org/10.1088/1361-6560/abb5c3>

Important note

To cite this publication, please use the final published version (if applicable).
Please check the document version above.

Copyright

Other than for strictly personal use, it is not permitted to download, forward or distribute the text or part of it, without the consent of the author(s) and/or copyright holder(s), unless the work is under an open content license such as Creative Commons.

Takedown policy

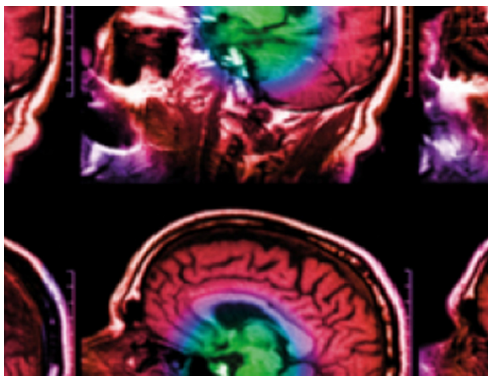
Please contact us and provide details if you believe this document breaches copyrights.
We will remove access to the work immediately and investigate your claim.

PAPER

Ultrasound transmission tomography image reconstruction with a fully convolutional neural network

To cite this article: Wenzhao Zhao *et al* 2020 *Phys. Med. Biol.* **65** 235021

View the [article online](#) for updates and enhancements.



IPEM | IOP

Series in Physics and Engineering in Medicine and Biology

Your publishing choice in medical physics,
biomedical engineering and related subjects.

Start exploring the collection—download the
first chapter of every title for free.



PAPER

Ultrasound transmission tomography image reconstruction with a fully convolutional neural network

Wenzhao Zhao¹ , Hongjian Wang², Hartmut Gemmeke³, Koen W A van Dongen⁴ , Torsten Hopp³ and Jürgen Hesser¹ ¹ Medical Faculty Mannheim, Heidelberg University, Theodor-Kutzer-Ufer 1-3, 68167 Mannheim, Germany² School of Computer Science and Technology, Donghua University, 2999 North Renmin Road, 201620 Shanghai, People's Republic of China³ Institute for Data Processing and Electronics, Karlsruhe Institute of Technology (KIT), Campus Nord, P.O. Box 3640, 76021 Karlsruhe, Germany⁴ Department of Imaging Physics, Delft University of Technology, Delft, The NetherlandsE-mail: hongjian.wang@dhu.edu.cn**Keywords:** breast cancer, ultrasound transmission tomography, image reconstruction, paraxial approximation, fully convolutional neural network**Abstract**

Image reconstruction of ultrasound computed tomography based on the wave equation is able to show much more structural details than simpler ray-based image reconstruction methods. However, to invert the wave-based forward model is computationally demanding. To address this problem, we develop an efficient fully learned image reconstruction method based on a convolutional neural network. The image is reconstructed via one forward propagation of the network given input sensor data, which is much faster than the reconstruction using conventional iterative optimization methods. To transform the ultrasound measured data in the sensor domain into the reconstructed image in the image domain, we apply multiple down-scaling and up-scaling convolutional units to efficiently increase the number of hidden layers with a large receptive and projective field that can cover all elements in inputs and outputs, respectively. For dataset generation, a paraxial approximation forward model is used to simulate ultrasound measurement data. The neural network is trained with a dataset derived from natural images in ImageNet and tested with a dataset derived from medical images in OA-Breast Phantom dataset. Test results show the superior efficiency of the proposed neural network to other reconstruction algorithms including popular neural networks. When compared with conventional iterative optimization algorithms, our neural network can reconstruct a 110×86 image more than 20 times faster on a CPU and 1000 times faster on a GPU with comparable image quality and is also more robust to noise.

1. Introduction

Breast cancer is one of the most commonly diagnosed cancers for females (Ferlay *et al* 2016, Fitzmaurice *et al* 2018). Early breast cancer detection increases the chance of curative treatment (Ruiter *et al* 2012). Ultrasound computed tomography (USCT) is a promising diagnostic tool in this respect. The method for tomographic imaging with transmission ultrasound (i.e. ultrasound transmission tomography, UTT) has been intensively studied in recent years. UTT can record the speed of sound and attenuation simultaneously. The speed of sound is shown to be closely related to tissue density (Glide *et al* 2007). It has been proved that by combining the speed of sound and attenuation images with reflection images, we can discriminate healthy tissue from cancer masses better than the diagnosis only based on the speed of sound or attenuation (Johnson *et al* 2007).

Transmission tomography involves solving the wave equation (the Helmholtz equation), which is associated with a heavy computational burden (van Dongen and Wright 2006, Taskin *et al* 2018, Kak *et al* 2002). To reduce the computational costs, approximation methods are used such as straight ray

approximation, bent ray approximation (Dapp 2013), Born approximation (Duric *et al* 2011), Rytov approximation (Simonetti *et al* 2009), and paraxial approximation (Dapp 2013). The straight ray approximation ignores refraction and diffraction, which leads to the worst image resolution (Althaus 2016). Among the above mentioned approximation methods, the paraxial approximation achieves the highest precision that is similar to full-wave solutions with the computational complexity reduced effectively (Taskin *et al* 2018). Recently, this approximation method has been combined with various optimization methods to accelerate the reconstruction (Wang *et al* 2019). However, this iterative optimization reconstruction strategy is sensitive to noise and needs regularization (Gemmeke *et al* 2016).

In recent years, deep learning has been demonstrated to improve the reconstruction of medical images. The state-of-the-art deep-learning-based medical image reconstruction falls into two categories: one is to combine deep learning with traditional algorithms to improve imaging quality, such as using deep learning as prior (or regularization) term (Jin *et al* 2017); or using neural networks as post-processing method for denoising, and artifact removal (Han and Ye 2018). The other category is neural-network-based direct image reconstruction from measurement data (Zhu *et al* 2018, Haggström *et al* 2019, Li *et al* 2019). One of the most successful algorithms in this category is Automap (Zhu *et al* 2018). It combines fully connected layers with convolutional layers for MRI image reconstruction, where the fully connected layers are used for domain transform while the convolutional layers are for extracting high-level features from the data and forcing the image to be represented sparsely in the convolutional-feature space. However, the fully connected layer requires a huge number of parameters for normal-size images, which makes Automap difficult for practical applications. In the field of ultrasound imaging, there has been research works on applying neural network for improving and accelerating the image reconstruction (Yoon *et al* 2018, Gao *et al* 2019). However, up to now, the research on deep-learning-based image reconstruction of transmission tomography is quite limited. The previous work in this respect yields a poor image quality with the neural network and involves fully connected layers to deal with small-size images only (Cheng *et al* 2019). In this work, we propose a fully learned image reconstruction approach using a fully convolutional neural network for UTT. The contributions of this paper are embodied in four aspects:

- We designed a neural network that can efficiently reconstruct the UTT image. The proposed reconstruction method overcomes the deficiency of fully connected neural networks and can work on normal-size inputs with a reasonable number of model parameters.
- We show the importance of advanced down- and up-scaling (DUS) methods for efficient image reconstruction by neural networks, which allows a larger number of parameters with a less computational burden.
- Compared with other state-of-the-art neural networks, the proposed neural network converges much faster in the training process and achieved a higher imaging quality.
- Compared with traditional algorithms, the proposed neural network is more robust to noise, at least 20 times faster on a CPU and 1000 times faster on a GPU. Its robustness to uncertainties in ultrasound transducer locations is also demonstrated.

2. Problem formulation

The transmission tomography problem can be expressed as the minimization of the following objective function:

$$J(\eta) = \|\mathcal{T}(\eta) - p\|_2^2 \quad (1)$$

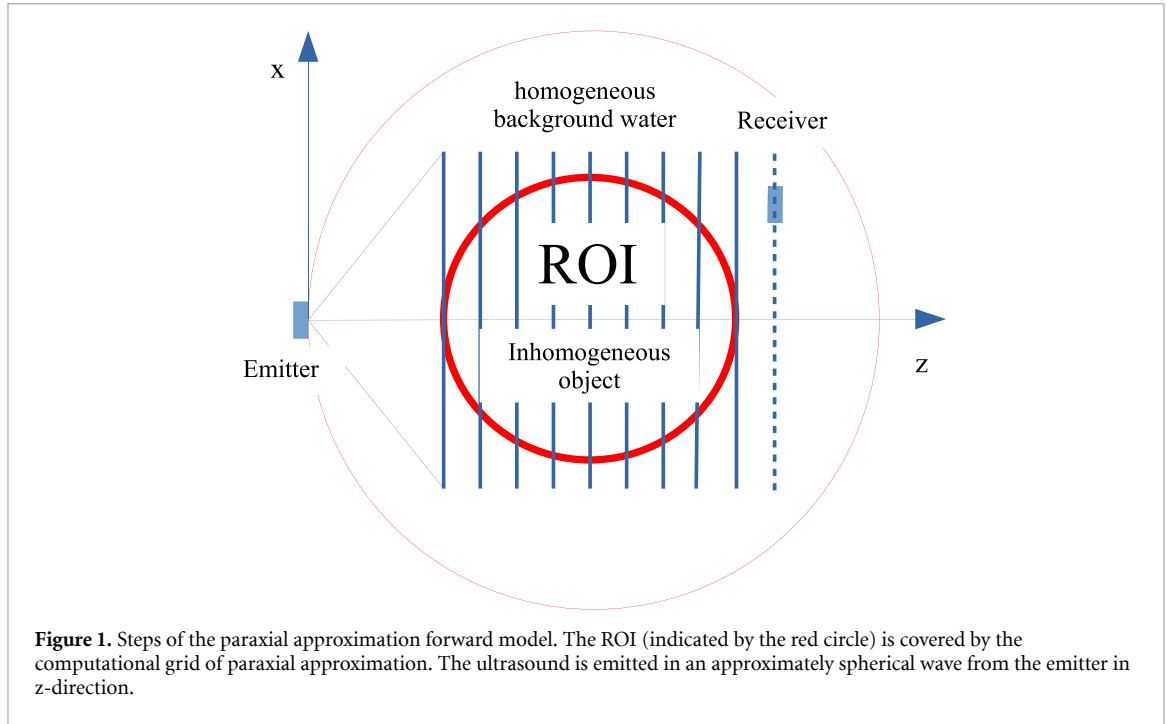
where $\eta \in X$ is the target image to be reconstructed and $p \in Y$ is the recorded data (frequency-dependent pressure field). X and Y are typically Hilbert Spaces, and the forward operator $\mathcal{T} : X \rightarrow Y$ models the relationship between the target image and the recorded data. In some conventional iterative algorithms, this inverse problem is often regularized by assuming that the reconstructed speed-of-sound (SoS) profile is smooth. The smooth constraint can be implemented by including the total variation (TV) of the reconstructed SoS vector $\|c\|_{TV}^2$ (Ramirez *et al* 2016, Ozmen *et al* 2015). Then we have

$$J(\eta) = \|\mathcal{T}(\eta) - p\|_2^2 + \lambda \|c\|_{TV}^2 \quad (2)$$

with weighting parameter λ .

As for the forward operator \mathcal{T} , we consider the wave equation in the frequency domain. The Helmholtz equation models the wave propagation of ultrasound through an acoustic background medium including refraction, diffraction, and multiple scattering as

$$\Delta p + k_0^2(1 + \eta)^2 p = 0 \quad (3)$$



where p describes pressure field in the frequency domain (i.e. the Fourier transform of the raw waveform data), and the background wave number $k_0 = \omega/c_0$ with angular frequency ω and the SoS of the background medium c_0 . The refractive index is $1 + \eta$ and $\eta = a + i\frac{\mu}{k_0}$ accounts for the deviation of the inhomogeneity from the background medium. Specifically, $\text{Re}(\eta) = a = \frac{c_0}{c} - 1$ is related to SoS, where c and c_0 are the SoS in the soft tissue and the background medium, respectively. $\text{Im}(\eta) = \frac{\mu}{k_0}$ depends on the parameter μ that accounts for frequency dependent attenuation with $i = \sqrt{-1}$.

The full solution of the Helmholtz equation poses a very high computational burden. In this paper we use hereby the paraxial approximation (Taskin *et al* 2018, Althaus 2016, Thomson *et al* 1983, Levy 2000, Saad and Lee 1986) which is faster to compute than the full-wave inversion.

According to Althaus (2016), we consider that the wave sources (i.e. the emitters) are arranged around a circle and the receivers (i.e. transducers) are put in a line at the opposite side of the emitters, where the relative position of the emitters and transducers is fixed. For each source, the wave propagates from a slice to its neighboring slice (as shown in figure 1), where the average ray direction is denoted by z . The forward propagation from the k th z slice to the $(k+1)$ th z slice on a 2D computational grid $[1, N_x] \times [0, N_z]$ with equidistant step width Δx and Δz can be calculated by the following equation:

$$p_{k+1} = e^{i\Delta z k_0 \eta_k} \cdot \mathcal{F}^{-1} \{ e^{i\Delta z \sqrt{k_0^2 - \xi^2}} \cdot \mathcal{F}(p_k) \}. \quad (4)$$

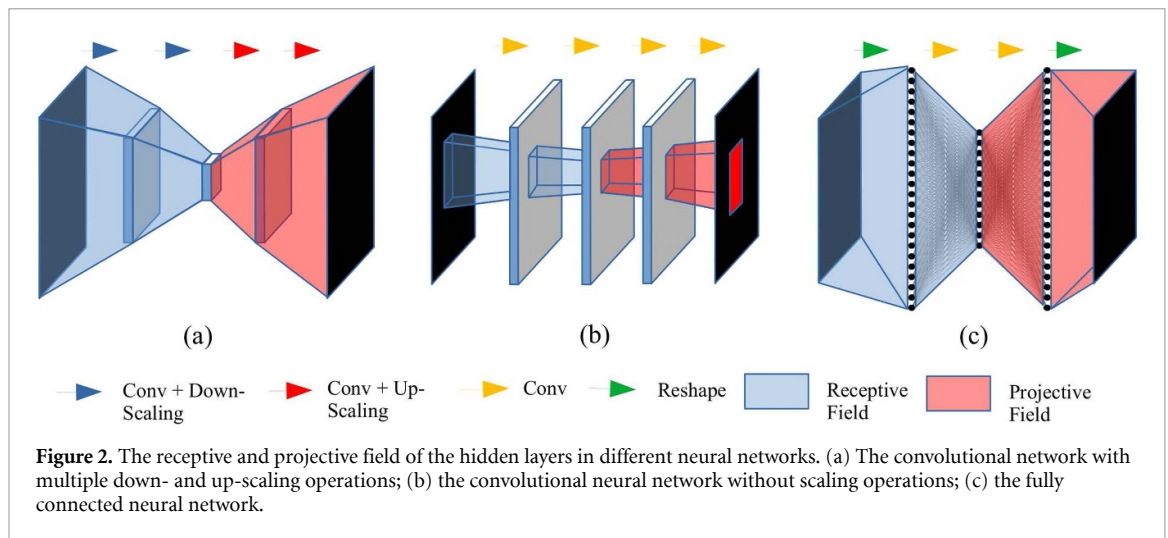
The index k at p and η represent the k th z slice. The spectral variable $\xi = \frac{2\pi}{\Delta x(N_x-1)} [-\frac{N_x}{2} + 1, \dots, 0, \dots, \frac{N_x}{2}]^T \in \mathbb{R}^{N_x}$. The 1D discrete Fourier transform with respect to the spatial coordinate x and the 1D inverse discrete Fourier transform are denoted by \mathcal{F} and \mathcal{F}^{-1} , respectively. For the emitter at different position of the circle, we rotate the computational grid around the region of interest (ROI) accordingly. Supposing we have NE emitters and NT transducers at the opposite position of each emitter and their relative positions are fixed, a full scan consists of $NE \times NT$ recorded waves.

Our objective in this paper is to achieve fully learned direct reconstruction of image η from data p , i.e. $\mathcal{T}^{-1} : Y \rightarrow X$ with a convolutional neural network only. The structure of the subsequent paper is organized as follows. We will show the network architecture and training strategy in section 3; the material and methods for experiments are illustrated in section 4; and the results in section 5; Finally, discussion and conclusion are put in section 6.

3. Network architecture and training strategy

3.1. Neural network architecture

For direct image reconstruction from recorded data, the value of each pixel is related to the measurement data from all sensors. Thus we need a neural network with a large receptive and projective field (Le *et al*



2017) that can cover the whole input sensor data and output image data. Recent work normally employs a fully connected neural network to obtain the maximum receptive and projective field (as shown in figure 2(c)). However, the fully connected neural network is limited to reconstructing small 2D images due to its large memory requirements. Apart from fully connected neural networks, a UNet (Ronneberger *et al* 2015) can be another option, which uses pooling units (for down-scaling) and unpooling units (for up-scaling) to gain a large receptive and projective field. However, the normal UNet uses low-pass filters such as max-pooling or average pooling methods to finish the downscaling operation. As demonstrated in Han and Ye (2018), Ye *et al* (2018), even though the UNet has by-pass connection to compensate for the loss of high frequency signal, it still emphasizes too much on the low-frequency signal because of the duplication of the low frequency branch. In Liu *et al* (2018), wavelet-based scaling methods are used to give more focus on high-frequency signals. However, as the wavelet transform is a special case of a convolutional layer, using the wavelet for down-scaling may limit the performance when compared with the case of using a trainable convolutional layer (Yu *et al* 2019). In this paper, we adopt a convolutional layer with a stride of 2 for tensor down-scaling as in Yu *et al* (2019), Haris *et al* (2018). The sub-pixel convolutional unit (Shi *et al* 2016) is used for up-scaling because of its low computational cost.

The overall architecture of the proposed neural network is shown in figure 3. The whole neural network is like a big U-shaped residual neural network containing 4 densely connected small DUS units that each forms a small U-shaped residual neural network. We hereby denominate the neural network as multiple W-net (mWnet for short). As a whole, the neural network comprises three parts: feature extraction, domain transform, reconstruction.

- **Initial feature extraction:** The convolutional layers with a stride of 2 are used to down-scale the feature map. At each scaling level, a residual block with nine convolutional layers (as shown in figure 3) is used to encode the feature map.
- **Domain transform:** Since the domain transform is mainly done by the ‘high level’ layers (i.e. the hidden layers processing highly down-scaled feature maps) with a large receptive and projective field, it is necessary to put more parameters to the ‘high level’ layers. Inspired by the deep-learning-based work in image denoising (Yu *et al* 2019, Abdelhamed *et al* 2019) and super-resolution (Haris *et al* 2018), we add multiple down- and up-scaling (DUS) units to gain the number of ‘high level’ layers. Since these ‘high level’ layers are used to process the highly scaled feature maps only, the filters from these layers are more computationally efficient than those filters in the ‘low level’ layers (i.e. the hidden layers processing feature maps with less downscaling). Inspired by the work of DenseNet (Huang *et al* 2017), we give a dense connection between these down- and up-scaling (DUS) units to further boost the performance. We use 1×1 convolutional layer for feature pooling and dimension reduction.
- **Reconstruction:** Immediately after the domain-transform part, we put a residual block after every up-scaling operation to reconstruct the image. We use sub-pixel convolutional layers to up-scale the features without degradation of features. With skip connection from the feature extraction part to the reconstruction part, we can reuse the extracted feature at different scaling levels to enhance the accuracy of reconstruction.

We refer to the network with 1 DUS unit as mWnet_1 and the network with 4 DUS units as mWnet_4. The size of input tensor is $2 \times 110 \times 128$ (110 transducers and 128 emitters), and the size of output tensor is

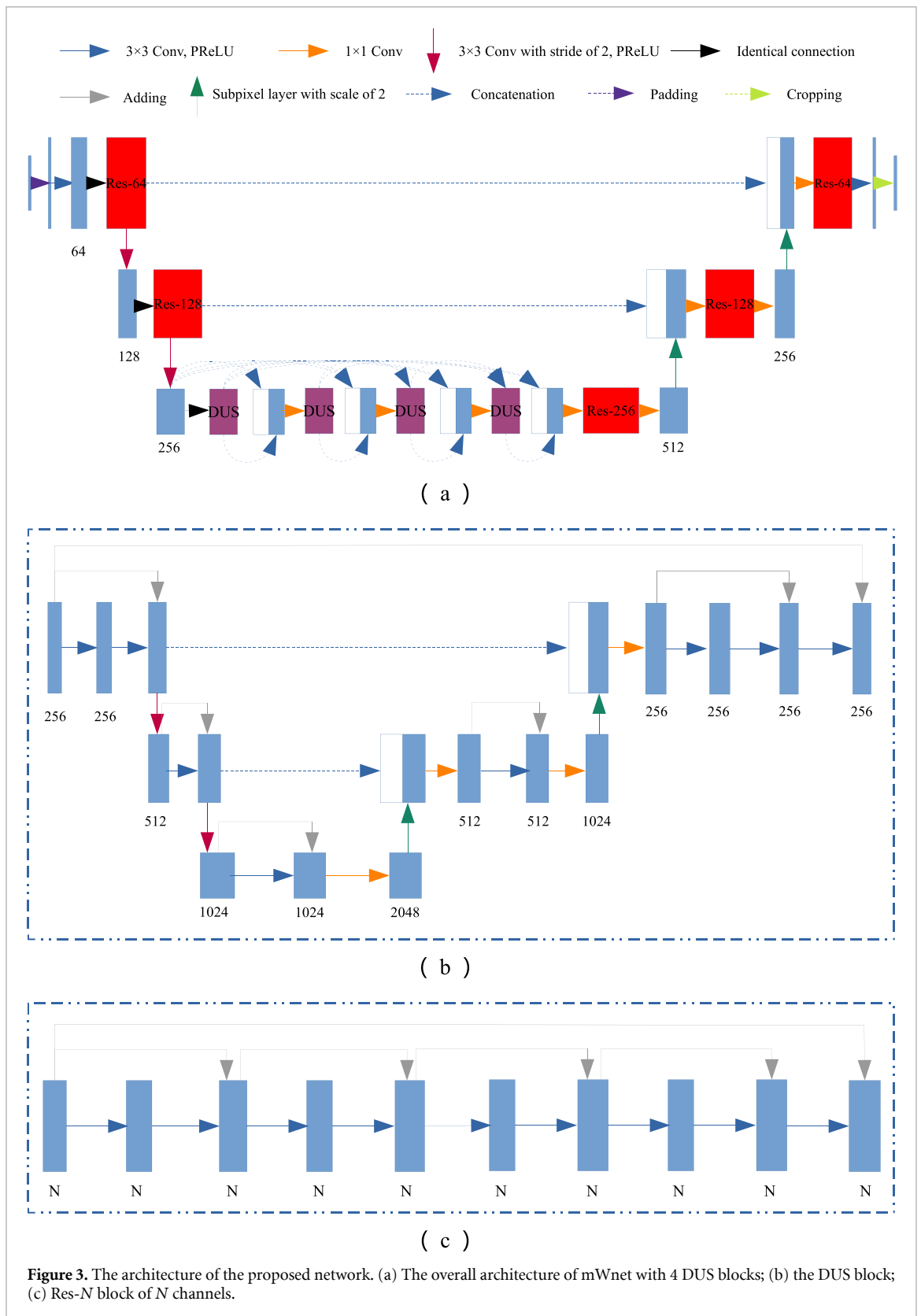


Figure 3. The architecture of the proposed network. (a) The overall architecture of mWnet with 4 DUS blocks; (b) the DUS block; (c) Res-N block of N channels.

$2 \times 110 \times 86$ (containing the real and imaginary part of η that are related to the SoS and attenuation, respectively). Before processed by convolutional layers, each input tensor is first padded into a $2 \times 128 \times 128$ tensor. After the processing of convolutional layers, each output tensor is obtained by cropping a $2 \times 128 \times 128$ tensor. The basic convolutional unit consists of one convolutional layer followed by PReLU (He et al 2015) activation function. We only use convolutional kernels with size = 3×3 or 1×1 . The total number of parameters for mWnet_1 and mWnet_4 are about 34.5 million and 113.6 million, respectively.

3.2. Training Strategy

The model is trained on the simulated data derived from natural images from ImageNet dataset (Deng *et al* 2009) using paraxial approximation forward model. In the training of the neural network, to augment the data and speed up the convergence (Audhkhasi *et al* 2016), random Gaussian noise is added to the input tensor with a probability of 0.7. As for the noise level, it should be noted that too high a noise level may affect the accuracy of the reconstruction, while an excessively low noise level (close to zero) cannot lead to a decent boost of convergence. Empirically, we set the SNR (Signal to Noise Ratio) range as 112–142 dB. Adam optimizer and l_1 loss are applied. For the implementation of l_1 loss, the real part and imaginary part of η are multiplied by a coefficient of τ and $1 - \tau$, respectively. We empirically set $\tau = 0.9$ for optimal training performance. To reduce the training time, we adopt the training strategy described in Smith *et al* (2017) by fixing the learning rate $lr = 1.0 \cdot 10^{-4}$ and increasing the batch size gradually. The model is first trained with a batch size of 16 for 49 epochs, then a batch size of 32 for 8 epochs, a batch size of 64 for 8 epochs, a batch size of 128 for 8 epochs, a batch size of 256 for 8 epochs, and finally a batch size of 512 for 8 epochs. To implement the training with a large batch size, we split a large batch of samples into a few mini-batches of size 16, and accumulate the gradients of these mini-batches before updating the variable.

To compare the neural networks with different numbers of DUS units, we implemented two different models in Pytorch (Paszke *et al* 2017): mWnet_1 with one DUS unit only, and mWnet_4 with 4 DUS units. The training of all these two models follows the same strategy. The training was performed on a server with GPU of NVIDIA TITAN XP, where the training of neural network mWnet_1 and mWnet_4 needed about 4.5 and 6.3 days, respectively.

For comparison, we further trained three other neural networks with the same training strategy: Automap, UNet, and FC-DenseNet103 (Jégou *et al* 2017). Both of these three neural networks have been used in the reconstruction of MRI images successfully (Chen *et al* 2019).

For the tests on uncertainties in transducer locations, the mWnet_4 trained using the above training strategy is further trained on the dataset simulated with perturbed settings and follows the same training strategy.

4. Material and methods

4.1. Data preparation

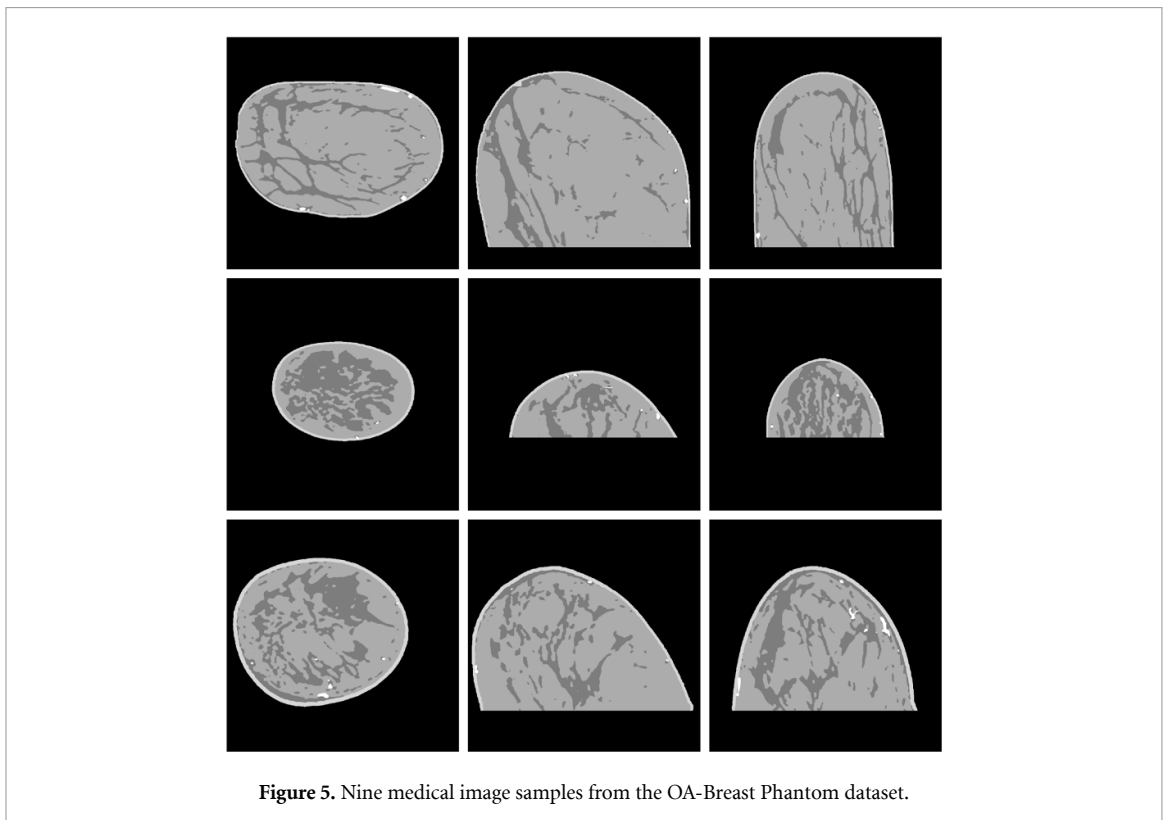
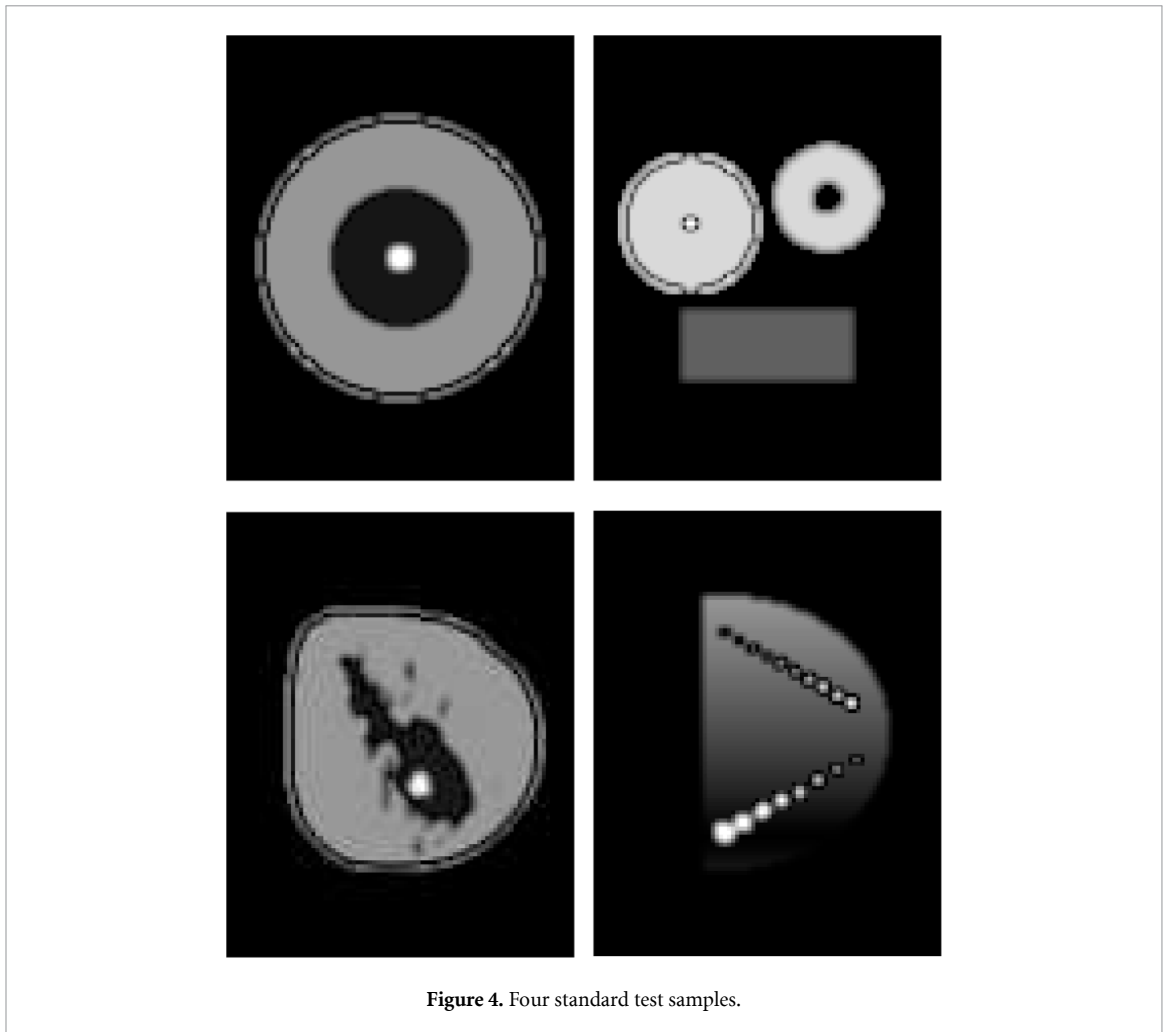
The image size for all phantoms is 110×86 with each pixel of size 1.88 mm, where the radius of the measuring device is 130 mm and the radius of the phantom is 79.7 mm, and 110 transducers and 128 emitters are simulated at the frequency of 0.5 MHz.

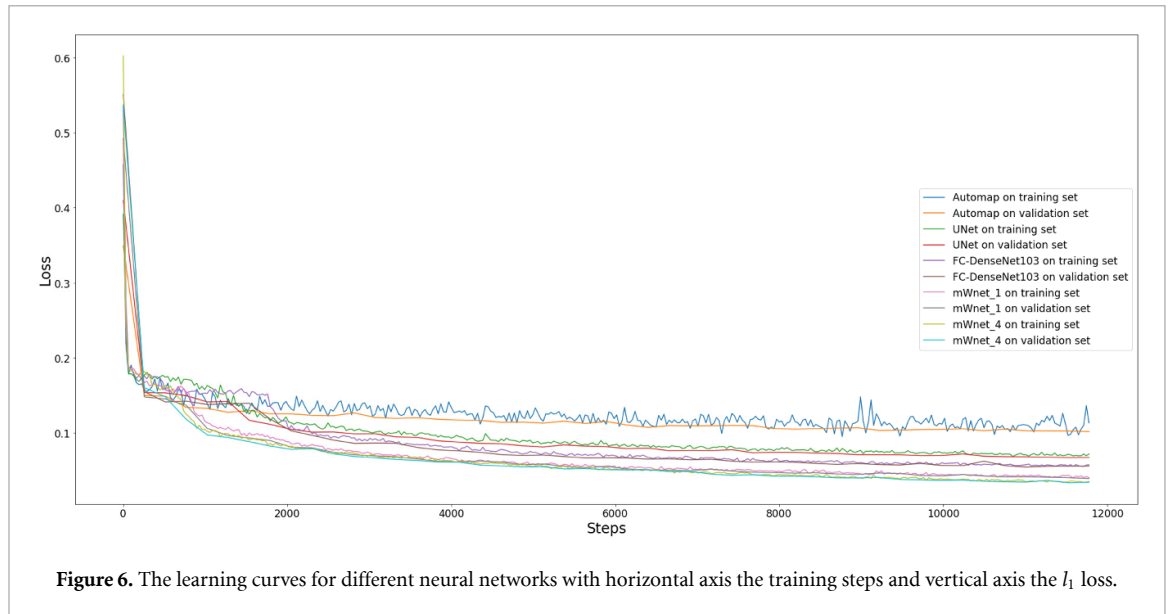
The natural images from ImageNet are used to generate training set and validation set. We obtain grayscale images with pixel value $x \in [0, 255]$ by extracting Y-channel luminance from the RGB color images. In total, 49,998 natural grayscale images are accumulated from ImageNet. Specifically, 47,998 images are used as training set. The size of the training set is further quadrupled by combining two data augmentation operations: grayscale-value reversing and 90 degree rotation. Considering any pixel with grayscale value x , the grayscale value is reversed as $255 - x$. Each image is then rotated through 90 degrees to double the size of the training set. After data augmentation, all the $47,998 \times 4$ images are scaled to a size of 110×86 . Then, for validation set, the remaining 2000 images are used and scaled to the same size. For any grayscale image derived from ImageNet set with value in the range of $[0, 255]$, its grayscale value is scaled and discretized into six integers i.e. 0, 1, 2, 3, 4 and 5 which represents water, skin, fat, gland, tumor, and calcification, respectively.

The test dataset comprises four standard test phantoms (as shown in figure 4) and nine medical images that are randomly selected from the OA-Breast Phantom dataset (Lou *et al* 2017) (as shown in figure 5). As for the nine medical images, the pixels for different tissues in the breast are labeled as: 0 for background, 2 for fibro-glandular tissue, 3 for fat, 4 for skin layer, and 5 for blood vessel. All the images are scaled to the size of 110×86 .

Given the image set with each tissue labeled, we assign the value of η for each pixel according to the property of SoS and attenuation for each tissue. Specifically, for water, skin, fat, gland, tumor, and calcification, the values simulated for SoS are 1485, 1570, 1450, 1490, 1560, and 6420 m s^{-1} , respectively; and the values simulated for attenuation are 0, 2.08, 1.26, 0.88, 1.60, and 8.0 dB/cm/MHz, respectively. The η image is then smoothed by a Gaussian filter so as to ensure that the area between different tissues has a smooth gradient of SoS and attenuation and thus becomes more realistic.

The measurement data collected by receivers (i.e. frequency-dependent sound pressure p in the frequency domain) is then calculated based on the η image and the paraxial approximation method for wave equation as described in Althaus (2016). The complex-valued measurement data (of size 110×128) is turned into a $2 \times 110 \times 128$ real input tensor. Finally, the element values of all the input tensors and target images are scaled to the range of (0, 1).



**Table 1.** The training time and number of parameters for different neural networks.

	Automap	UNet	FC-DenseNet103	mWnet_1	mWnet_4
Training time (days)	4.6	2.1	4.7	4.5	6.3
Number of parameters (million)	356.0	7.8	9.3	34.5	113.6

Table 2. The average runtime per image for different algorithms.

	Newton CG	L-BFGS	Automap	UNet	FC-Dense Net103	mWnet_1	mWnet_4		
Runtime	49.1 min (CPU)	24.9 s (CPU)	0.011 s (GPU)	0.008 s (GPU)	0.014 s (GPU)	0.778 s (CPU)	0.012 s (GPU)	1.056 s (CPU)	0.018 s (GPU)

To test the algorithms' robustness to uncertainties in transducer locations, we generate another set of measurement data based on all the above-mentioned η images and the paraxial approximation method by adding random additive white Gaussian noise to transducers' location parameters. Specifically, we add zero-mean white Gaussian noise of standard variance 0.02° to the rotation angle, and we add zero-mean white Gaussian noise of standard variance 0.01 mm to both the x value and the z value (as shown in figure 1) of each receiver.

4.2. Performance evaluation

Imaging quality is quantified using two standard metrics: normalized root mean square error (NRMSE) and structure similarity (SSIM). The NRMSE is defined as:

$$NRMSE = \sqrt{\frac{\sum_{i=1}^M \sum_{j=1}^N [x(i,j) - y(i,j)]^2}{MN(x_{\max} - x_{\min})^2}} \quad (5)$$

where x and y denote the ground truth and the reconstructed image, respectively. M and N are the number of pixels for row and column, respectively. x_{\max} and x_{\min} are the maximal and minimal pixel value of the ground truth image, respectively.

The SSIM is defined as:

$$SSIM = \frac{(2\mu_y\mu_x + c_1)(2\sigma_{yx} + c_2)}{(\mu_y^2 + \mu_x^2 + c_1)(\sigma_y^2 + \sigma_x^2 + c_2)} \quad (6)$$

where μ_y is an average of y , σ_y^2 is a variance of y , and σ_{yx} is a covariance of y and x . There are two variables to stabilize the division such as $c_1 = (k_1L)^2$ and $c_2 = (k_2L)^2$. L is a dynamic range of the pixel intensities. k_1 and k_2 are constants with $k_1 = 0.01$ and $k_2 = 0.03$ by default.

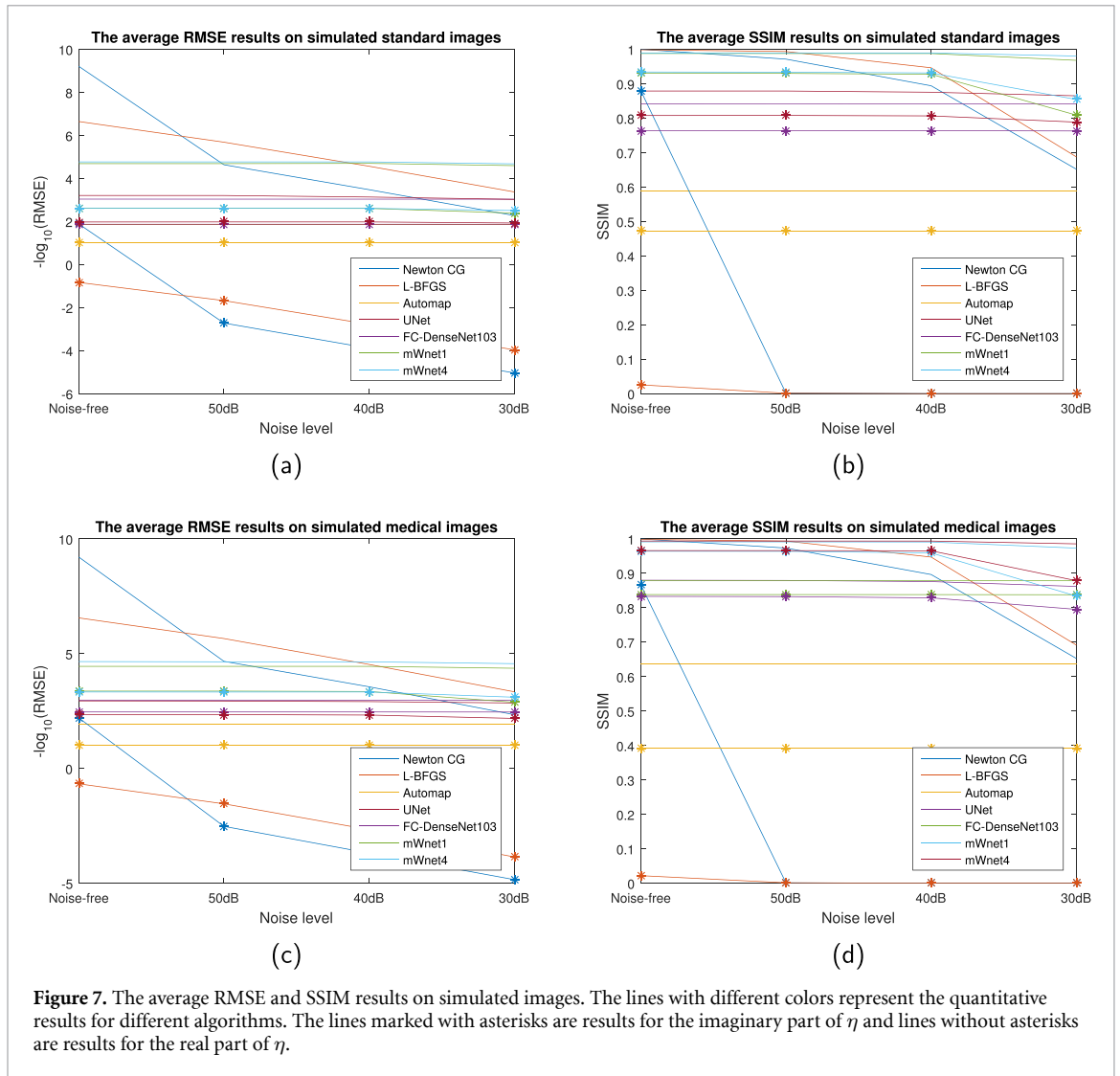


Figure 7. The average RMSE and SSIM results on simulated images. The lines with different colors represent the quantitative results for different algorithms. The lines marked with asterisks are results for the imaginary part of η and lines without asterisks are results for the real part of η .

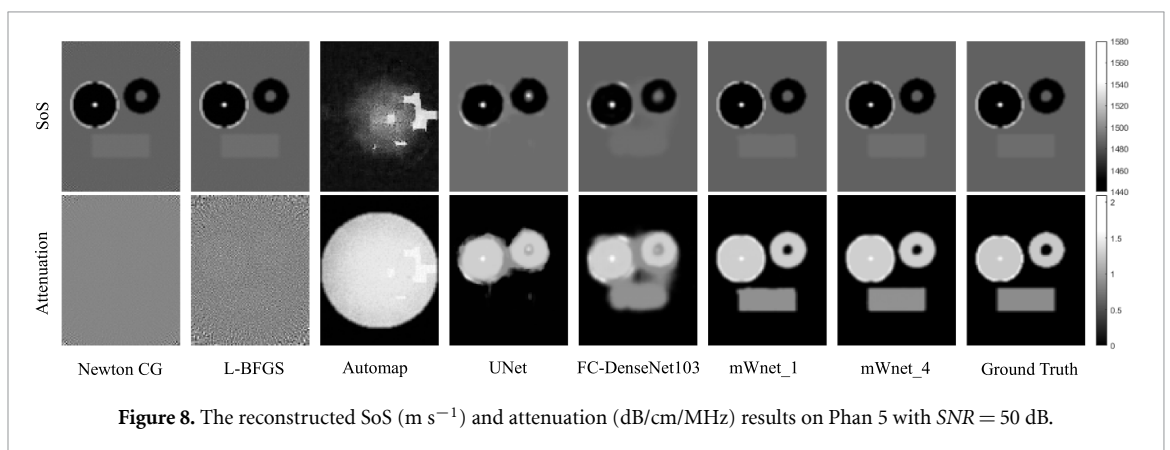
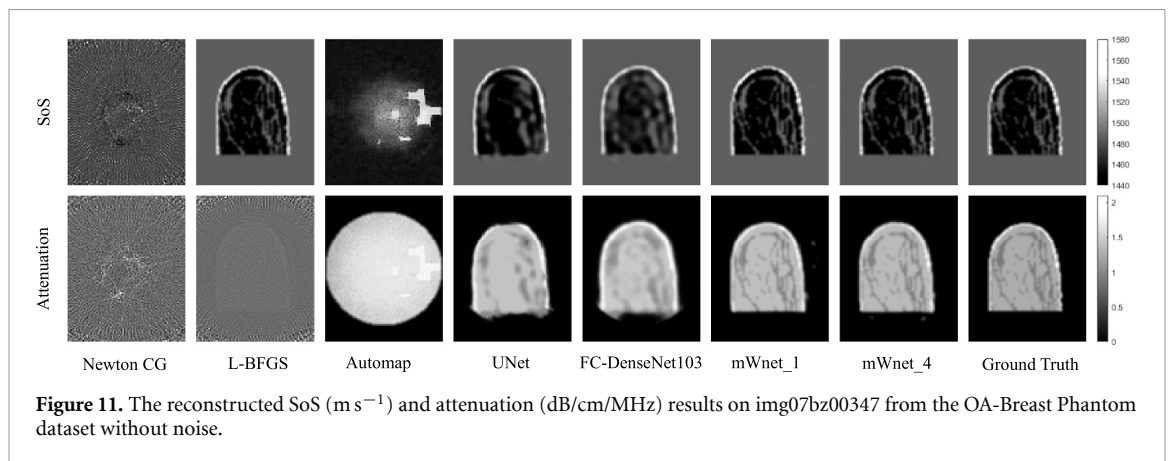
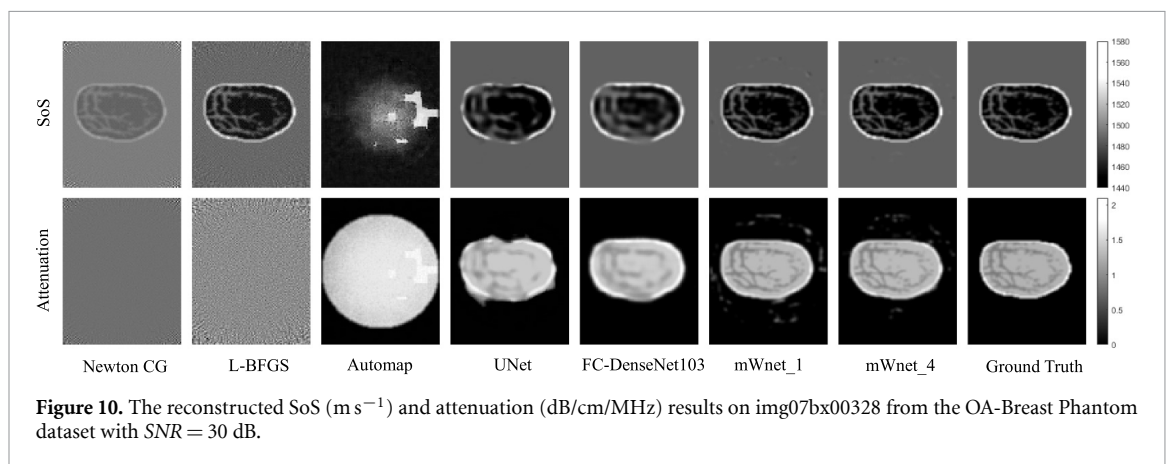
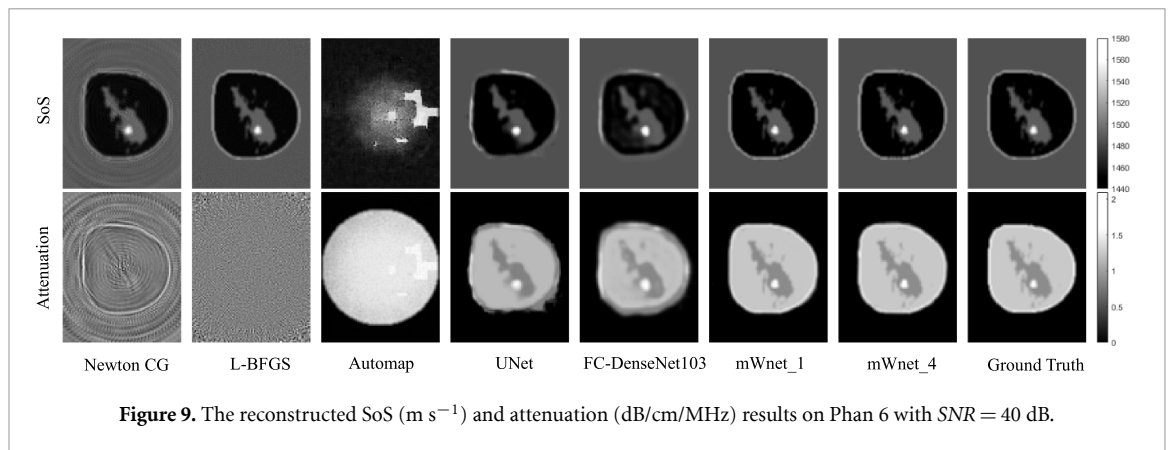


Figure 8. The reconstructed SoS (m s^{-1}) and attenuation (dB/cm/MHz) results on Phan 5 with $\text{SNR} = 50 \text{ dB}$.

5. Results

We compare mWnet_1 and mWnet_4 with three neural networks: Automap, UNet, and FC-DenseNet, and two other traditional reconstruction algorithms that use different optimization methods: Gauss Newton CG (Gemmeke *et al* 2016) and L-BFGS (Wang *et al* 2019) on a laptop with CPU Intel Core i5 8400 2.80GHz and GPU Nvidia GeForce RTX 2070. All the algorithms are tested with their optimal default settings, where the maximum iteration numbers for Gauss Newton CG and L-BFGS are 500 and 100, respectively.



The learning curves for different neural networks are displayed in figure 6. We see that the proposed neural networks converge much faster than other algorithms. Table 1 shows the general training time and number of parameters. The average runtime per image for different algorithms is shown in table 2. We see that compared with traditional algorithms, deep-learning-based algorithms are much faster on CPU. Running on GPU can further speed up the deep-learning-based reconstruction significantly. Even though the number of parameters of mWnet_4 is about 3 times as large as that of mWnet_1, the increase of runtime of mWnet_4 is less than a factor of two. This is because the additional parameters in mWnet_4 lie only in the DUS units that process the down-scaled tensors.

The quantitative results are presented in figure 7 for both the four standard test images and the medical images derived from the OA-Breast Phantom dataset. We have the input data corrupted by Additive white Gaussian noise at 4 different noise levels with the signal-noise-ratio $\text{SNR} = 30, 40, 50$ dB and noise-free, respectively. As a whole, the neural network is more robust to noise and can reconstruct both the real part and imaginary part well, while the traditional algorithms can only reconstruct noisy real part and the

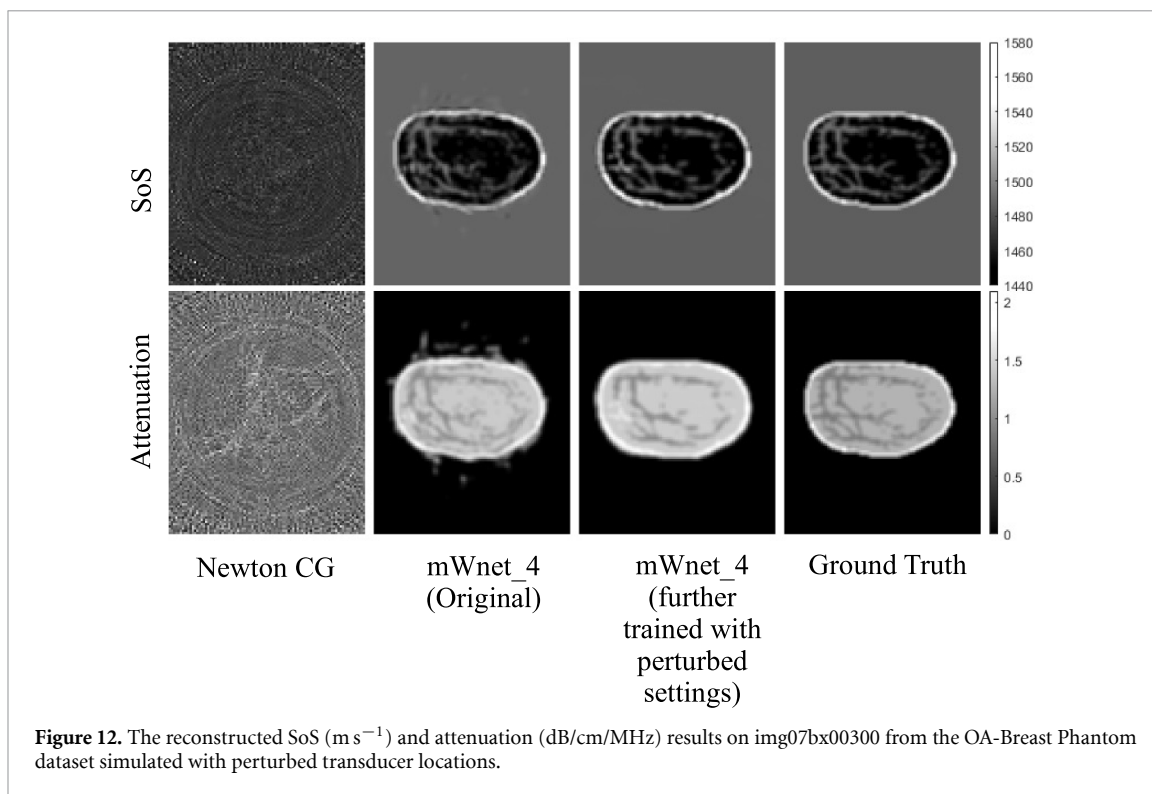


Figure 12. The reconstructed SoS (m s^{-1}) and attenuation (dB/cm/MHz) results on img07bx00300 from the OA-Breast Phantom dataset simulated with perturbed transducer locations.

imaging quality decreases significantly with the increase of noise. In addition, it can be noted that mWnet_4 is more robust to noise than mWnet_1, especially at a high noise level such as $SNR = 30$ dB.

The visual results for standard test samples and the medical images at different noise levels are shown in figures 8–11, which verify the proposed neural network's superior imaging quality for noisy inputs. Specifically, on the one hand, for the reconstruction of the real part of η , image quality by mWnet is comparable to that by traditional algorithms for noise-free cases, and mWnet is superior to the traditional algorithms at a high noise level (i.e. $SNR = 30$ dB in figure 10). On the other hand, for the reconstruction of the imaginary part, mWnet can always achieve a decent visual performance, while traditional algorithms normally fail to reconstruct a meaningful image in the presence of noise.

In addition, mWnet_4 has much better visual performance than mWnet_1 for noisy cases. For example, in figure 8, the sides of the rectangular are straight in the result for mWnet_4 but are distorted in the result for mWnet_1; in figure 10, mWnet_1 has more artifacts than mWnet_4.

Figure 12 shows mWnet_4's robustness to uncertainties in transducer locations compared with Gauss Newton CG. With more training on the dataset simulated with perturbed settings, the mWnet_4's imaging quality is improved further.

6. Discussion and conclusion

The proposed neural networks show superior imaging quality to any other neural networks including the Automap, FC-DenseNet, and the classical UNet. Among these three neural networks, the Automap is the most inefficient one with the worst imaging quality and the highest number of parameters due to the use of fully connected layers. On the other hand, the fully convolutional neural networks FC-DenseNet and UNet have the smallest number of parameters but only yield a blurred result. Meanwhile, the proposed neural networks show the highest imaging quality and maintain an acceptable inference speed. Compared with the other two popular convolutional neural networks FC-DenseNet and UNet, the factors that lead to mWnet's superior performance in both imaging quality and efficiency are: 1) As demonstrated in the section of Network Architecture and Training Strategy, the proposed neural networks use advanced down-scaling and up-scaling operators, which give more emphasis on the high-frequency part of the data; 2) The proposed neural networks iteratively implement multiple down- and up-scaling operator to gain the number of layers with large receptive and projective field, which also allows the efficient implementation of a large number of parameters.

The results show that with more DUS units in the hidden layers, the neural network obtains a higher imaging quality and becomes more robust to noise, which is also confirmed by the works in Yu *et al* (2019),

Haris *et al* (2018). Although the increase of the number of DUS units leads to a significant increase in model size, it is still much smaller than the neural network using fully connected layers, and the computational burden is controlled in an acceptable range. The multiple down-up scaling strategy allows the neural networks to implement more parameters efficiently with much lower computational burden. It is also possible to extend the mWnet to dealing with larger-size 2D or 3D images by putting more scaling operations to both the initial feature extraction part and the reconstruction part. This kind of extension ensures that the size of the feature maps processed by DUS units is within the receptive field and projective field of hidden layers in DUS units. Adding more scaling operations will increase a tiny number of parameters and help control the computational burden within a reasonable range. Apart from the number of scaling operations in the initial feature extraction part and the reconstruction part, the number of DUS units in mWnet should also be changed based on experiments.

The traditional algorithm Gauss Newton CG gives a result much better than the result by L-BFGS for the noise-free test cases. It is because of their different settings on initialization, step length, and iterative number, which make the implementation of Gauss Newton CG more suitable for noise-free cases. Meanwhile, we also see that these conventional algorithms all perform better than mWnet on noise-free cases. One reason for this phenomenon is that Gauss Newton CG and L-BFGS use exactly the same forward model for simulation to iteratively optimize the solution, while neural network only learns the solution indirectly via the dataset generated based on the forward model and ends up yielding an approximate solution. When training dataset is increased, this gap between the traditional algorithms and neural networks can be narrowed further.

It should be noted that the traditional iterative optimization algorithms (Gauss Newton CG and L-BFGS) are often stuck into various local optimal solutions in the presence of noise or uncertainties in transducer location, while the neural network can obtain an approximation solution that is closer to the global solution easily. Meanwhile, the fully learned neural network approach is also much faster than the iterative optimization approaches. However, in the case of low noise level, the neural network is inferior to traditional algorithms in terms of imaging accuracy. For higher imaging accuracy of the neural network, one solution is to enlarge the training set or to involve medical images into the training set for finetuning. In addition, the imaging quality can be further improved by using the neural network to get a good initialization for traditional optimization.

Since the wave-based transmission tomography has high degrees of scattering due to the long wavelength at the scale of the objects, the UTT image reconstruction has higher complexity than Radon inversion in the straight-ray-based tomography (such as x-ray CT) and is of high non-linearity, the favorable performance of the proposed neural network on UTT image reconstruction proves its potential to tackle other image reconstruction problems such as CT and MRI image reconstruction.

In the future work, we will continue investigating how to improve the efficiency of the neural network further to deal with large-size images. We will also test the proposed neural networks on real data from different imaging tasks.

Acknowledgments

This work was supported by the Deutsche Forschungsgemeinschaft (DFG) under Grant Nos. HE 3011/37-1 and HO 5565/2-1, the Fundamental Research Funds for the Central Universities from Donghua University under Grant No. 20D111205, and the Young Teacher Research Startup Fund from Donghua University under Grants No. 112-07-0053079.

ORCID iDs

Wenzhao Zhao  <https://orcid.org/0000-0001-5150-3781>

Koen W A van Dongen  <https://orcid.org/0000-0001-6711-5898>

Jürgen Hesser  <https://orcid.org/0000-0002-4001-1164>

References

- Abdelhamed A, Timofte R and Brown M S 2019 Ntire 2019 challenge on real image denoising: methods and results 2019 *IEEE/CVF Conf. on Computer Vision and Pattern Recognition Workshops (CVPRW)* pp 2197–2210
- Althaus L 2016 On acoustic tomography using paraxial approximations *MS thesis* Darmstadt University of Technology, Department of Mathematics
- Audhkhasi K, Osoba O and Kosko B 2016 Noise-enhanced convolutional neural networks *Neural Netw.* **78** 15–23

- Chen Y, Shaw J L, Xie Y, Li D and Christodoulou A G 2019 Deep learning within a Priori temporal feature spaces for large-scale dynamic MR image reconstruction: application to 5-D cardiac MR multitasking *Medical Image Computing and Computer Assisted Intervention - MICCAI 2019 MICCAI 2019* (Lecture Notes in Computer Science vol 11765) (Cham: Springer) pp 495–504
- Cheng A, Kim Y, Anas E M, Rahmim A, Boctor E M, Seifabadi R and Wood B J 2019 Deep learning image reconstruction method for limited-angle ultrasound tomography in prostate cancer *Proc SPIE* **10955** 1095516
- Dapp R 2013 Abbildungsmethoden für die Brust mit einem 3D-Ultraschall-Computertomographen *PhD thesis* Institut für Prozessdatenverarbeitung und Elektronik (IPE) (<https://doi.org/10.5445/IR/1000037036>)
- Deng J, Dong W, Socher R, Li L J, Li K and Fei-Fei L 2009 Imagenet: a large-scale hierarchical image database *2009 IEEE Conf. on Computer Vision and Pattern Recognition* pp 248–55
- Duric N, Li C, Roy O and Schmidt S 2011 Acoustic tomography: promise versus reality *2011 IEEE Int. Ultrasonics Symp.* pp 2033–41
- Ferlay J et al 2013 GLOBOCAN 2012: Estimated Cancer Incidence, Mortality and Prevalence Worldwide in 2012 v1.0 *IARC CancerBase No. 11*
- Fitzmaurice C et al 2018 Global, regional, and national cancer incidence, mortality, years of life lost, years lived with disability, and disability-adjusted life-years for 29 cancer groups, 1990 to 2016: a systematic analysis for the global burden of disease study *JAMA Oncol.* **4** 1553–68
- Gao Z, Wu S, Liu Z, Luo J, Zhang H, Gong M and Li S 2019 Learning the implicit strain reconstruction in ultrasound elastography using privileged information *Med. Image Anal.* **58** 101534
- Gemmeke H, Althaus L, Van Dongen K W, Egger H, Hesser J, Mayer J, Rüter N V, Zapf M and Hopp T 2016 Wave equation based transmission tomography *2016 IEEE Int. Ultrasonics Symp. (IUS)* pp 1–4
- Glide C, Duric N and Littrup P 2007 Novel approach to evaluating breast density utilizing ultrasound tomography *Med. Phys.* **34** 744–53
- Han Y and Ye J C 2018 Framing U-Net via deep convolutional framelets: Application to sparse-view CT *IEEE Trans. Med. Imaging* **37** 1418–29
- Haris M, Shakhnarovich G and Ukita N 2018 Deep back-projection networks for super-resolution *2018 IEEE/CVF Conf. on Computer Vision and Pattern Recognition* pp 1664–73
- He K, Zhang X, Ren S and Sun J 2015 Delving deep into rectifiers: Surpassing human-level performance on imagenet classification *2015 IEEE Int. Conf. on Computer Vision (ICCV)* pp 1026–34
- Huang G, Liu Z, Van Der Maaten L and Weinberger K Q 2017 Densely connected convolutional networks *2017 IEEE Conf. on Computer Vision and Pattern Recognition (CVPR)* pp 2261–9
- Häggström I, Schmidlein C R, Campanella G and Fuchs T J 2019 DeepPET: A deep encoder-decoder network for directly solving the PET image reconstruction inverse problem *Med. Image Anal.* **54** 253–62
- Jin K H, McCann M T, Froustey E and Unser M 2017 Deep convolutional neural network for inverse problems in imaging *IEEE Trans. Image Process.* **26** 4509–22
- Johnson S, Abbott T, Bell R, Berggren M, Borup D, Robinson D, Wiskin J, Olsen S and Hanover B 2007 Non-invasive breast tissue characterization using ultrasound speed and attenuation *Acoustical Imaging* (Dordrecht: Springer) pp 147–54
- Jégou S, Drozdal M, Vazquez D, Romero A and Bengio Y 2017 The one hundred layers tiramisu: fully convolutional densenets for semantic segmentation *2017 IEEE Conf. on Computer Vision and Pattern Recognition Workshops (CVPRW)* pp 1175–83
- Kak A C, Slaney M and Wang G 2002 Principles of computerized tomographic imaging *Med. Phys.* **29** 107–107
- Le H and Borji A 2017 What are the receptive, effective receptive, and projective fields of neurons in convolutional neural networks? (arXiv: 1705.07049)
- Levy M 2000 *Parabolic Equation Methods For Electromagnetic Wave Propagation* (Stevenage: IET) p 45
- Li Y, Li K, Zhang C, Montoya J and Chen G H 2019 Learning to reconstruct computed tomography images directly from sinogram data under a variety of data acquisition conditions *IEEE Trans. Med. Imaging* **38** 2469–81
- Liu P, Zhang H, Zhang K, Lin L and Zuo W 2018 Multi-level wavelet-CNN for image restoration *2018 IEEE/CVF Conf. on Computer Vision and Pattern Recognition Workshops (CVPRW)* pp 886–09
- Lou Y, Zhou W, Matthews T P, Appleton C M and Anastasio M A 2017 Generation of anatomically realistic numerical phantoms for photoacoustic and ultrasonic breast imaging *J. Biomed. Opt.* **22** 041015
- Ozmen N, Dapp R, Zapf M, Gemmeke H, Rüter N V and van Dongen K W 2015 Comparing different ultrasound imaging methods for breast cancer detection *IEEE Trans. Ultrason. Ferroelectr. Freq. Control* **62** 637–46
- Paszke A, Gross S, Chintala S, Chanan G, Yang E, DeVito Z, Lin Z, Desmaison A, Antiga L and Lerer A 2017 Automatic differentiation in PyTorch *31st Conference on Neural Information Processing Systems (NIPS 2017)*
- Ramirez A B and van Dongen K W 2016 Sparsity constrained contrast source inversion *J. Acoust. Soc. Am.* **140** 1749–57
- Ronneberger O, Fischer P and Brox T 2015 U-Net: Convolutional networks for biomedical image segmentation *International Conference on Medical Image Computing and Computer-assisted Intervention* (Cham: Springer) pp 234–41
- Rüter N, Zapf M, Dapp R, Hopp T and Gemmeke H 2012 First in vivo results with 3D ultrasound computer tomography *2012 IEEE Int. Ultrasonics Symp.* pp 1–4
- Saad Y and Lee D 1986 *A New Algorithm For Solving The Wide Angle Wave Equation* (Yale University. Department of Computer Science) pp 1–15
- Shi W, Caballero J, Huszár F, Totz J, Aitken A P, Bishop R, Rueckert D and Wang Z 2016 Real-time single image and video super-resolution using an efficient sub-pixel convolutional neural network *2016 IEEE Conf. on Computer Vision and Pattern Recognition (CVPR)* pp 1874–83
- Simonetti F, Huang L and Duric N 2009 A multiscale approach to diffraction tomography of complex three-dimensional objects *Appl. Phys. Lett.* **95** 061904
- Smith S L, Kindermans P J, Ying C and Le Q V 2017 Don't decay the learning rate, increase the batch size (arXiv: 1711.00489)
- Taskin U, Ozmen N, Gemmeke H and van Dongen K W 2018 Modeling breast ultrasound; on the applicability of commonly made approximations *Arch. Acoust.* **43** 425–35
- Thomson D J and Chapman N 1983 A wide-angle split-step algorithm for the parabolic equation *J. Acoust. Soc. Am.* **74** 1848–1854
- van Dongen K W and Wright W M 2006 A forward model and conjugate gradient inversion technique for low-frequency ultrasonic imaging *J. Acoust. Soc. Am.* **120** 2086–95
- Wang H, Gemmeke H, Hopp T and Hesser J 2019 Accelerating image reconstruction in ultrasound transmission tomography using L-BFGS algorithm *Proc. SPIE* **10955** 109550B
- Ye J C, Han Y and Cha E 2018 Deep convolutional framelets: A general deep learning framework for inverse problems *SIAM J. Imaging Sci.* **11** 991–1048

- Yoon Y H, Khan S, Huh J and Ye J C 2018 Efficient b-mode ultrasound image reconstruction from sub-sampled rf data using deep learning *IEEE Trans. Med. Imaging* **38** 325–36
- Yu S, Park B and Jeong J 2019 Deep iterative down-up CNN for image denoising *2019 IEEE/CVF Conf. on Computer Vision and Pattern Recognition Workshops (CVPRW)* pp 2095–103
- Zhu B, Liu J Z, Cauley S F, Rosen B R and Rosen M S 2018 Image reconstruction by domain-transform manifold learning *Nature* **555** 487